

Developable Rotationally Symmetric Kirigami-Based Structures as Sensor Platforms

Erin E. Evke, Dilara Meli, and Max Shtein*

Developable surfaces based on closed-shape, planar, rotationally symmetric kirigami (RSK) sheets approximate 3D, globally curved surfaces upon (reversible) out-of-plane deflection. The distribution of stress and strain across the structure is characterized experimentally and by finite-element analysis as a function of the material and cut parameters, enabling the integration with strain gauges to produce a wearable, conformal patch that can capture complex, multi-axis motion. Using the patch, real-time tracking of shoulder joint and muscle behavior is demonstrated. The facile fabrication and unique properties of the RSK structures potentially enable wearable, textile-integrated joint monitoring for athletic training, wellness, rehabilitation, feedback control for augmented mobility, motion of soft and traditional robotics, and other applications.

1. Introduction

Wearable activity and heart monitors have proliferated in the marketplace, creating an unprecedented data stream and opportunities for improving cardiovascular health and athletic performance. Joint movement, however, remains poorly quantified, while joint injuries dramatically impair function and raise the cost of healthcare. Nearly two million people in the U.S. enter the medical system just for rotator cuff injuries, with corresponding repair surgeries exceeding \$3 billion per year, while the annual market for orthopedic braces exceeds \$5 billion.^[1] Over 120 million Americans (one in two adults) are affected by painful or disabling bone, joint or muscular conditions,^[2] which often occur from improper positioning during active and/or passive activities, (e.g., weightlifting, sitting, and sleeping with bad posture). The cost of treatment and lost wages is estimated at over \$200 billion.^[2,3] Therefore, development of tools for in situ assessment and better understanding of joint movement could unlock a new frontier of using body kinematics to improve health span, athletic performance, gesture control of motion assistive devices, and enable many other applications.


Measurements of joint function typically involve the manual use of a goniometer to determine the range of motion.^[4] Some joints (e.g., shoulder) exhibit complex motion that is poorly assessed by a simple goniometer, in which the accuracy can

vary by as much as 45%.^[5,6] In sports, exercise, common tasks, and post-injury recovery, the process for achieving a desired range of motion requires professional assessment^[5] and a strict rehabilitation regimen,^[7] often hampered by poor adherence, resulting in poor patient outcomes. The ability to quantify movement of key joints during activity can dramatically improve outcomes for rehabilitation and boost athletic performance. However, directly monitoring and providing feedback on joint movement during an activity, unobtrusively and cost effectively, remain a major challenge.^[8–10]

Currently, tracking motion or deducing impact stresses is performed using camera motion tracking systems^[11,12] or inertial measurement units (IMUs) that consist of an accelerometer, gyroscope, and magnetometer, typically packaged in a rigid brace or integrated within a band or suit.^[13–15] In an attempt to improve the wearable aspect of the sensors, collection of positional data has been shown using conductive textiles, where special fibers integrated into the textile are the sensing elements.^[16–21] However, the sensing is based on stretching of the fibers, typically unidirectional and poorly suited for integration with substantially rigid electronic components that do not tolerate well to repeated mechanical deformation. Furthermore, the integration of electronic function into textiles remains a nonstandard, expensive process. Instead, an approach is needed where the device is flexible and curved, conforming to the body surface in use, yet is also flat and nonstretchable during fabrication to be compatible with dominant, scalable manufacturing and integration processes for electronics.

To resolve the conflicting design requirements stated above, we use closed-shape, planar kirigami structures, nominally with rotational symmetry, such as shown in **Figure 1**. Kirigami (Japanese art of cutting) has increasingly been used to engineer global elasticity in materials.^[22–25] The addition of cutting allows for greater control over the geometric design and system behavior.^[26] Recently, this has been leveraged to enable locomotion via soft actuators^[27] and flexible electronics.^[28–31] While technologies to generate patterns and functional coatings in two dimensions are now highly evolved, the structures examined here are easily generated at the application-appropriate length scales using a laser or die cutter. As the structure is displaced normal to its original plane, concentric rings defined by the cut lengths bend to create a combination of saddles with alternating positive and negative Gaussian curvatures. A sufficiently dense and appropriately configured cut pattern enables

E. E. Evke, D. Meli, Prof. M. Shtein
Department of Materials Science and Engineering
University of Michigan
Ann Arbor, MI 48109, USA
E-mail: mshtein@umich.edu

 The ORCID identification number(s) for the author(s) of this article can be found under <https://doi.org/10.1002/admt.201900563>.

DOI: 10.1002/admt.201900563

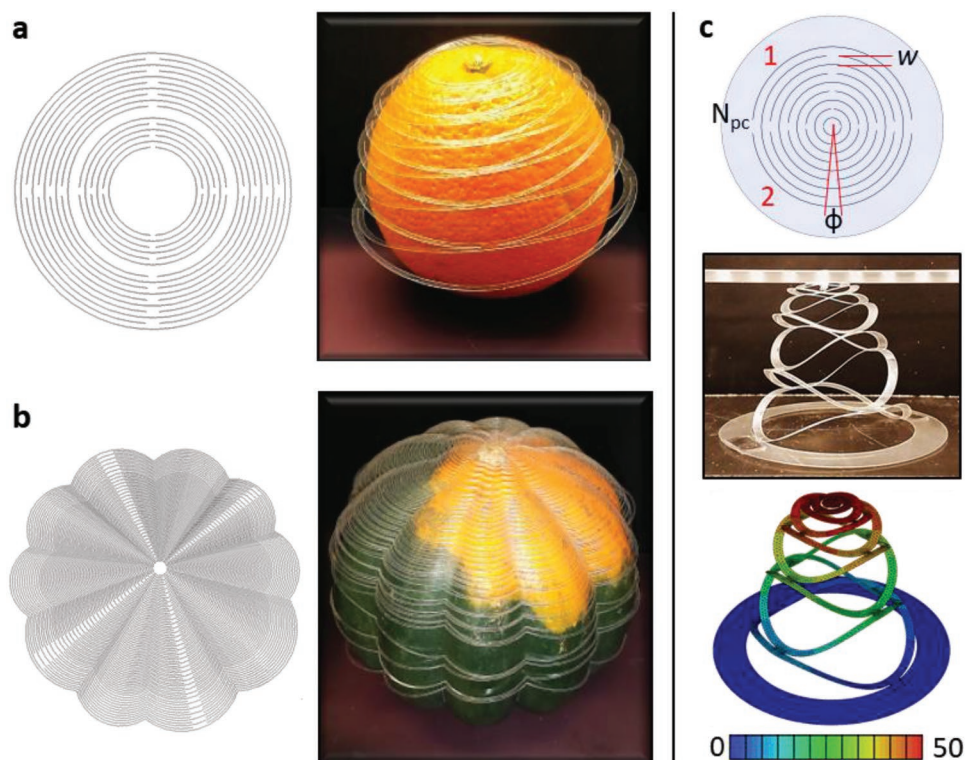


Figure 1. RSK structures approximating different curved surfaces. a) RSK springs assume the shape of an orange and b) an acorn squash; schematic of cut pattern on the left and physical model on the right. c) Baseline cut pattern delineating the cut parameters and deformation states of the physical and FEA model displaced to 50 mm (color bar indicates displacement in mm).

the structure to achieve large deflections and to conform to an envelope shape of complex curvature. We leverage the alternating local curvature—and therefore strain—to strategically place strain sensors and enable the quantification of joint movement.

2. Results and Discussion

Cut patterns were designed by following the contours of objects to enable wrinkle-free 3D transformations of planar sheets, allowing them to assume globally curved surfaces. For demonstration, cut patterns were tuned to match the curvatures of an orange and acorn squash (Figure 1a,b, respectively). The deformation behavior of these nominally rotationally symmetric kirigami (RSK) structures is governed by the radial spacing (w), angular spacing (ϕ), and the number of cuts along the perimeter of each concentric circle (N_{pc}) (Figure S1, Supporting Information). A classification system used to define the rotational symmetry of these patterns based on N_{pc} is shown in Figure S2 (Supporting Information). The cut patterns made in this study remain circular or ellipsoidal, symmetric about the central axis.

The basic element of RSK structures can be discretized by a series of beams, in which the segments between the cuts act as hinges, creating saddle points, as shown in Figure 1c, in which the color bar represents displacement in millimeters. Test specimens were made here using laser-cut polyethylene terephthalate (PET) sheets for convenience and cost-effectiveness, sufficient to represent the behavior of other materials, e.g.

such as those used for flexible printed circuit boards. (While circular and ellipsoidal cuts are analyzed here, it is understood that other base cut patterns may be used to better tune the deformed structure to the curvature, as represented in more detail in Figure S3 in the Supporting Information.)

2.1. Mechanical Testing

The mechanical response of the RSK platform was modeled using finite-element analysis (FEA), in which cross-plane, uniaxial forces were applied, and then plotting the logarithmic force versus displacement (Figure 2). The FEA models match well with experimental results in the linear elastic regime, as shown by the comparison of out-of-plane behavior in the inset images of Figure 2. The RSK structure can undergo large global displacements to beyond 1500× its original profile, as shown in the second inset of Figure 2. (A simplified model of the structure's behavior assumes segments of rings in which the total displacement of the structure is the summation of the displacement of each ring, as represented in the model in Figure S4 (Supporting Information). The more rings within a given area and perimeter, the larger the linear displacement limit of the spring.) Note that while the regimes in the force versus displacement plots are designated as linear or nonlinear, from close examination of the deformation, it is clear that most of the strain and stress (Figure S5, Supporting Information) is localized to the cut ends, which are thus more prone to plastic deformation. Indeed, beyond a displacement of ≈ 90 mm for

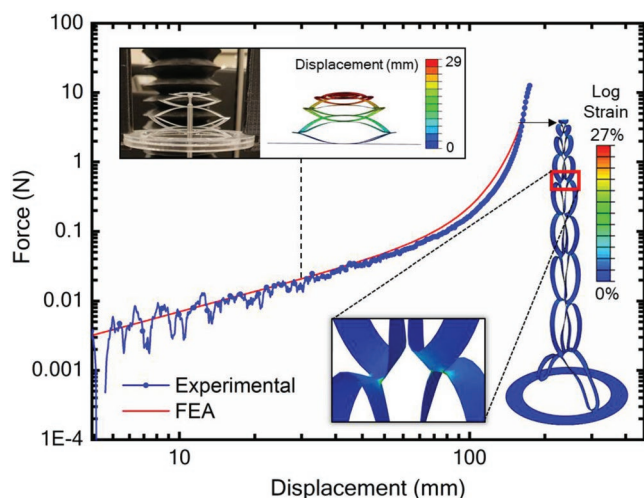


Figure 2. Experimental and FEA force–displacement curve for baseline pattern. Overlaid images above the curve show experimental and FEA samples deflected at 29 mm. Insets to the right and below depict FEA results at a large displacement of 152 mm and closeup image of local strain, at a concentrated force of 5 N; color bar represents logarithmic strain (%).

the structure in Figure 2, slight deviation between our FEA and experiment begins, attributed to the FEA models' assumption of purely elastic behavior, which has neglected plastic strain or strain-hardening that may occur at large displacements.

Figure 3 plots experimentally quantify force versus displacement to demonstrate the influence of w , ϕ , and N_{pc} on the mechanical properties. For constant angular and radial spacing, as the number of cuts along the perimeter increases, so too does the force required to displace the structure (Figure 3a). Similarly, increasing ϕ (Figure 3b) or increasing w (Figure 3c) requires more force to deflect the spring. Cantilever beam theory can be used to gain a better intuition of how the spaces between cuts act as beams and how beam geometry influences the mechanical properties such as yield displacement, as shown in Figure S6 (Supporting Information),^[32] albeit in the elastic regime in the strict sense. The smaller the number of cuts in the radial direction, or the larger the number of azimuthal cuts, the stiffer the beams and thus the higher the overall stiffness of the RSK structure in cross-plane deformation.

2.2. RSK Structure as Platform for Sensing

We take advantage of the alternating curvatures exhibited by the structure and introduce electronic components in the regions suitable to their deformation requirements and tolerances. For example, rigid sensors can be placed between the cut ends on the kirigami sheet, where there is minimal curvature upon deflection. Strain gauges, on the other hand, can be placed at points of greater local curvature (e.g., near the start of the cut). This integration principle allows the RSK structures to act as a multifunctional platform for the placements of a variety of otherwise substantially rigid or flexible sensor components. As a proof of concept, simple strain gauges are embedded on the RSK platform, oriented off-axis to each other, located near the cut ends (see schematic in **Figure 4a**). The combined

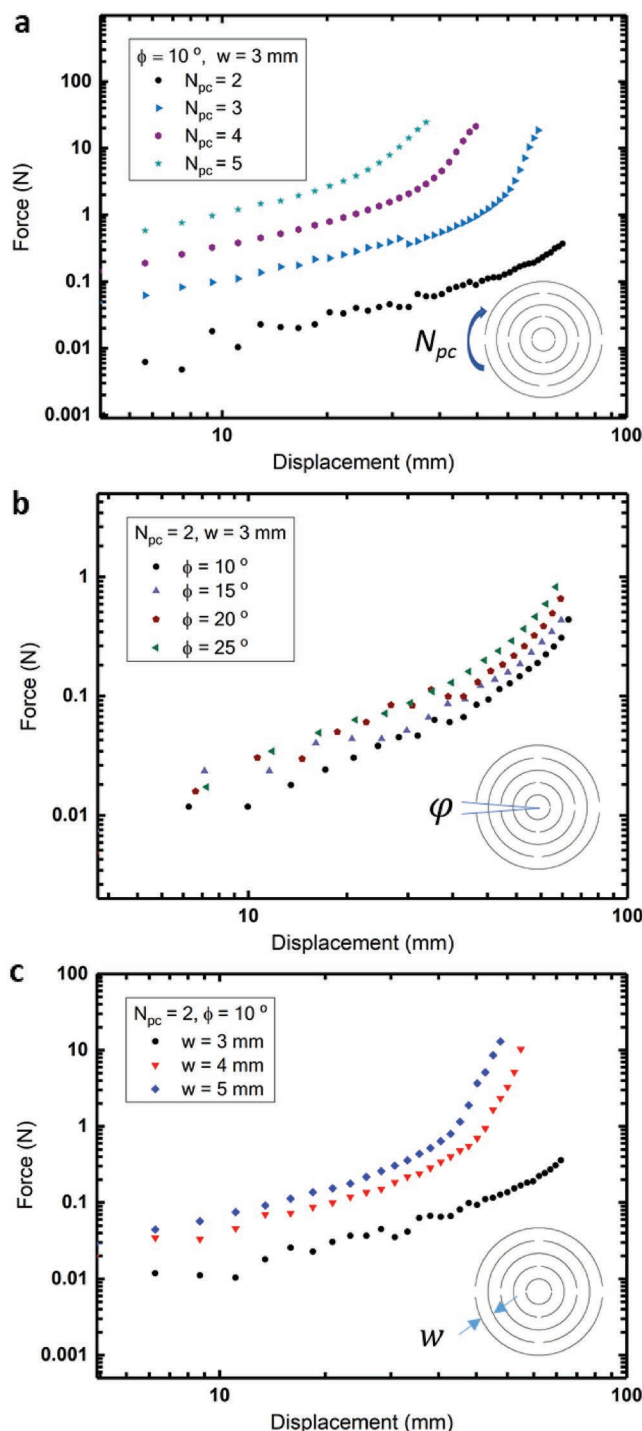


Figure 3. Logarithmic force versus displacement of various cut patterns. The mechanical properties are depicted comparing different cut patterns. Varying a) number of cuts along the perimeter, b) angular spacing, and c) radial spacing.

substrate and strain gauges are adhered onto the shoulder using a stretchy fabric adhesive used often in physical therapy; a cross-section is represented in **Figure 4b**. The placement of the sensors at the start and end of the cuts helps maximize the signal, as shown in **Figure 4c**, where a subunit ring is deformed

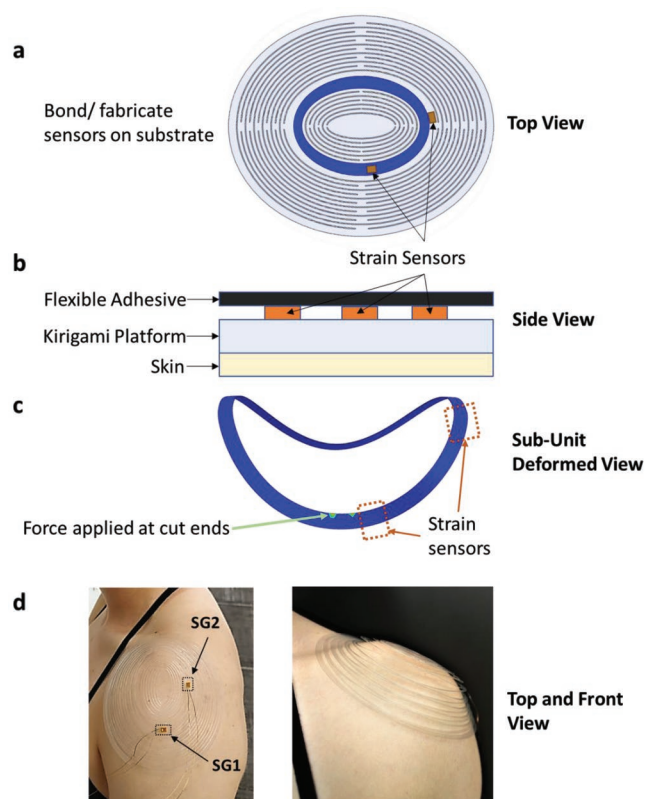


Figure 4. Placement of strain sensors on RSK platform. a) Top view of cut kirigami spring based on geometry of shoulder. b) Cross-sectional view of RSK-based device depicting the locations of sensing elements with respect to the kirigami platform, flexible adhesive, and skin. c) Sub-unit ring deformed shows the placement of strain sensors placed at the maximum degrees of curvature, which is at the start and ends of the cuts. d) Top and front views of device with bonded strain gauges placed on subject's shoulder without adhesive tape.

using FEA, with force applied at the cut ends in the inner part of the ring; an orange box indicates the location of the sensors. (A more detailed representation of the model is shown in Figure S4 in the Supporting Information.) In Figure 4d, the platform is shown placed on the shoulder of a user, where SG# represents a linear strain gauge. The flexible adhesive was omitted in the images in Figure 4d to show how the RSK device assumes the topology of the subject's shoulder, and how the sensor platform is oriented along the top of the shoulder.

To capture shoulder joint motions, one strain gauge is positioned outside of the acromion, in the vicinity of the greater tubercle of humerus/deltoid to capture the significant change in elevation upon raising the arm. Another sensor is placed along the back of the shoulder (e.g., along or near the supraspinatus or infraspinatus) to capture arm movement across the body. The cut pattern used for this subject has a radial spacing of $w = 1$ mm (except for the spacing of the rings that hold the strain sensors), an angular spacing of $\phi = 5$ mm, and $N_{pc} = 2$ (two cuts along the perimeter). Narrow yet long beams allow for the structure to be flexible enough to adapt to changes in the surface topology of the shoulder as the arm moves. The cut pattern can also be tuned to match variations in shoulder geometries, e.g., for broader shoulders an increase in the number of rings.

The device shown in Figure 4d was placed on the shoulder, and the subject performed various motions. The strain gauges experience changes in the local strain, altering their electrical resistance, captured by a control unit. An example of the collected and processed data is shown in Figure 5, where the correlation is made between the position of the limbs (and joint), and signals from the sensor(s) as the subject raises the arm up and down following the humeral elevation plane. (For corroboration by conventional multipoint motion tracking, trackers were placed in specific locations on the user's body to accurately track the positions of the upper body via a 19-camera motion capturing system that surrounds the user.)^[12] The coordinate system used to define the angular positions of the shoulder are depicted in the left skeleton diagram in Figure 5a. The humeral elevation angle is based on the plane parallel to the side of the body, humeral plane of elevation is the plane from the top view of the shoulder, and rotation of the shoulder joint, shown in Figure S7 in the Supporting Information and described more fully in ref. [11].

The skeletal representations of the user performing the raising arm motion, obtained by the camera tracking system, demonstrates the neutral position (left) and arm raised to 140° (right). A 3D plot of the elevation angle captured by the camera system is shown in Figure 5b, plotted against the resistance of two strain gauges, and versus time. The humeral plane of elevation angle and rotation remained relatively stable as the arm was raised and lowered along the humeral elevation angle (θ), with slight changes due to human error. The plateau sections in the beginning and end of the motion correspond to the subject standing still in the neutral position, with the arm by the side against the body, as indicate in the top panel of Figure 5c. The device maintains good contact with the shoulder throughout the motion as shown when the arm is raised at 79° and 120° in the middle and bottom images of Figure 5c, respectively. Since the adhesive tape is applied when the arm is in the neutral state, at higher elevation angles the adhesive tape begins to fold in the areas not occupied by the sensor platform. Nevertheless, the device maintained conformability to the shoulder. Overall, the correspondence between the motion performed and the change in resistance is evident with respect to the elevation angle and permits the use of strain gauge signals to compute motion.

Figure 6 captures the signals produced by other various shoulder motions, including circumduction and rotation. Figure 6a shows the subject circling the arm backward along the humeral elevation plane. SG1 more closely follows the motion corresponding to changes in the elevation angle, because it is located parallel to the beam bending in the direction of the performed motion. The angular velocity of the arm during these tests ranged from 0.16 to 1.7 rad s^{-1} . In addition to sensing relative changes in angular position, it also indicates acceleration as depicted in Figure 6b. The sequence starts with the user in a neutral position and then proceeds to run (in place), eventually slowing down to a walk and finishing back to the neutral position. (A video showing the skeleton movement in real time synchronized to the $\Delta R/R$ plots of Figures 5b and 6a,b can be found in the Supporting Information and may help gain a better sense of the characteristics of the elevation change, circumduction, and running sequences.)

Intriguingly, the RSK sensing device can also detect muscle flexion and contraction associated with more subtle movements,

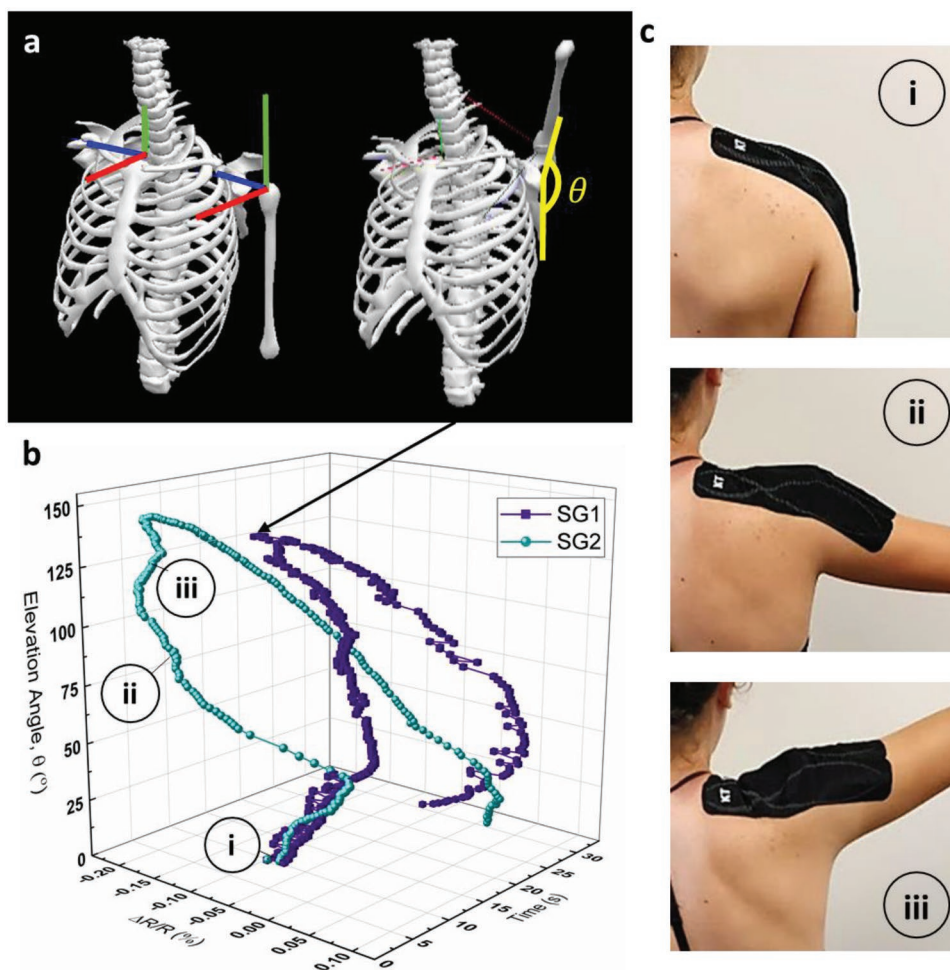


Figure 5. Tracking motion of raising and lowering arm. a) Skeleton representation of body at neutral position and skeleton with arm raised up to 140° with coordinate system used by the image processing software and elevation angle, θ . b) 3D plot representing elevation angle as a function of change of resistance and time in seconds. c) Kirigami sensing device at 0°, 79°, and 120°, represented in (i), (ii), and (iii), respectively.

including those of other joints in the arm. For example, changes in resistance are prominent during wrist rotation, which is controlled by muscles surrounding the shoulder (Figure 6c). For the wrist rotation activity, the subject raised the arm forward 90° from the body, horizontal to the floor, and rotated the wrist back and forth, causing the muscles in the shoulder to flex and contract. Changes in resistance and the associated angular positions associated with the motion of shrugging shoulders at various speeds are depicted in Figure 6d and for moving the arm across the body in Figure S8 (Supporting Information).

3. Summary and Conclusions

Planar, developable, rotationally symmetric kirigami structures were demonstrated to closely conform to surfaces with complex 3D curvature. The impact of cut geometry on the mechanical behavior of the cut structure was quantified using experiments and FEA. The alternating local Gaussian curvature—and therefore strain—between cuts was used to strategically place strain gauges on the RSK structure, permitting the

direct monitoring of motion of a complex joint (shoulder) in a unique, markerless motion tracking system. Simple, commercially available linear strain gauges were used to create a sensing device in a wired configuration, but scalable, monolithic integration using this platform can be cost-effective^[28] and would facilitate the use of additional sensors, wireless communications and power transfer. These results indicate that the RSK structures constitute a highly promising platform for the integration of a variety of sensing technologies in a wearable form factor for highly modular and multifunctional health and movement monitoring devices, using well-established manufacturing processes.

4. Experimental Section

Fabrication of RSK Springs and Acrylic Rings Using Laser Cutter: The circular kirigami patterns were fabricated by cutting 8.5" × 11" sheets of PET, 901 Highland Laser Printer Film (3M, 90 μm) with a 50 W Universal Laser Systems CO₂ laser cutter (5% power, 10% speed, and 1.5" optics). The Young's modulus and Poisson's ratio of the film is 2.2 GPa and 0.37, respectively. The overall diameter of the patterns was 75 mm with

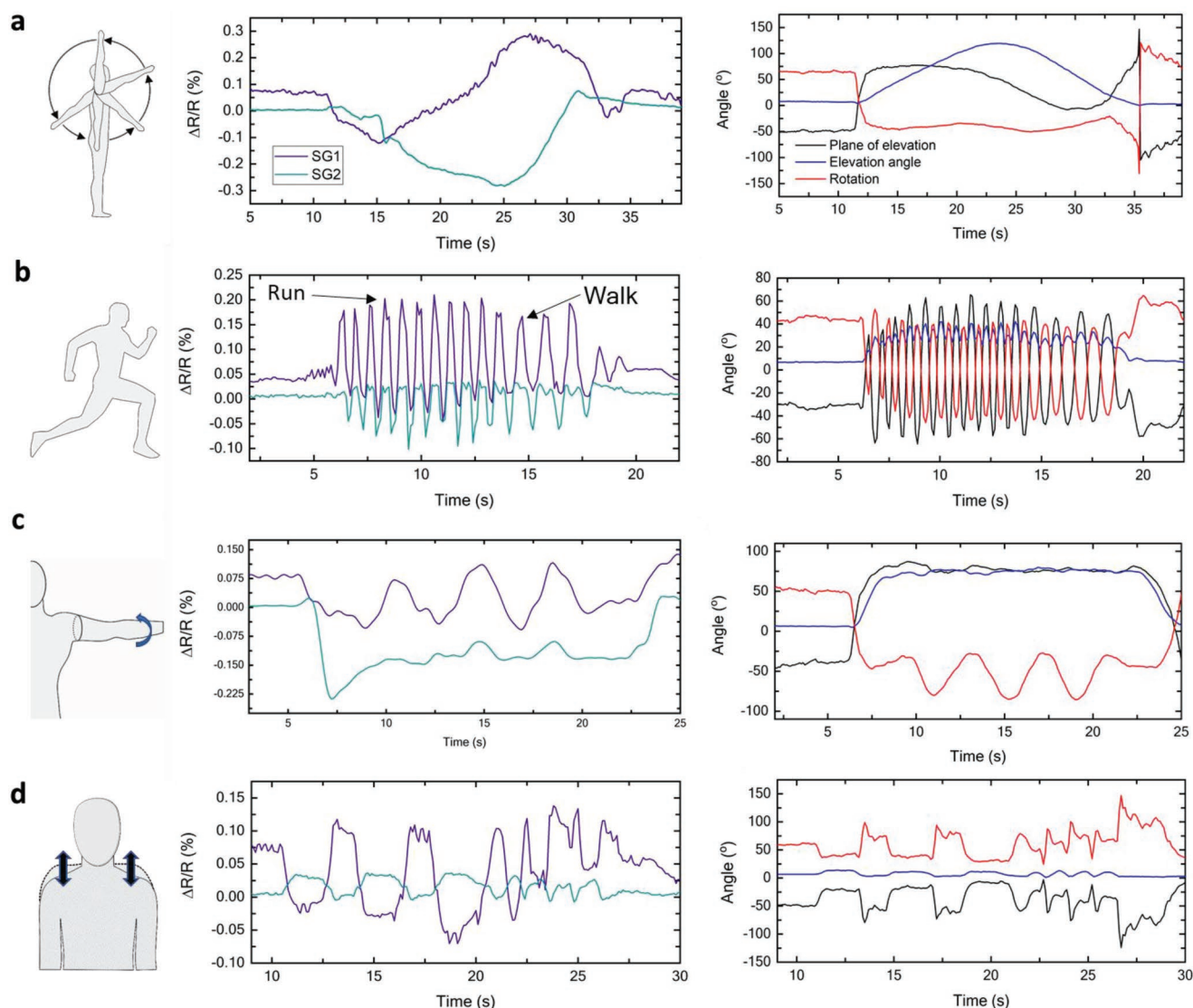


Figure 6. Changes in resistance and corresponding angular positions as various motions are performed. From left to right: schematic of motion performed, plot of change of resistance versus time for two linear strain gauges placed on the RSK substrate, and a plot of the angular positions as a function of time. The three defining planes and axis of motion is plane of elevation angle, elevation angle, and rotation. a) Arm circle backward, b) running, c) arm rotation, and d) shrugging shoulders.

the largest cut radius at 27 mm. For the data collected in Figures 4–6, the overall diameter of the patterns was 48 mm. For mechanical testing, two rings were cut from optically clear cast acrylic sheets (McMaster-Carr, 7/64" thick) with the laser cutter (100% power, 5% speed, and 2.0" optics) to hold and align the RSK springs during experimental tests. The noise within the experimental data at lower forces is due to the resolution of the equipment and the plotted data is smoothed in OriginPro.

Mechanical Testing of RSK Springs: The force and displacement curves were obtained at a strain rate of 5 mm s^{-1} via a TA.XTPlus Texture Analyzer (Texture Technologies, Hamilton, Massachusetts, USA) with a 30 kgf load cell and the Exponent (Texture Technologies, Hamilton, Massachusetts, USA) software package.

Finite-Element Modeling of RSK Springs: The software package Abaqus was used to model the elastic behavior of the RSK springs, based on the static, general method with a six-node linear triangular prism element (C3D6) mesh construction, using the nonlinear geometry option. The matrix storage is unsymmetric and the time incrementation step interval is 0.003–1 with a step size of 1×10^{-36} . Pinned boundary conditions are

used and the concentrated point loads are applied to the springs, as demonstrated in Figure S4 (Supporting Information).

Tracking Sensor: PET was laser-cut as mentioned above according to the measured geometry of the subject's shoulder. Linear strain gauges (350 Ω resistance, 2.14 gauge factor) from Omega Engineering were bonded to PET using Devcon high-strength 5 min epoxy and cured for 1 h at room temperature. Wires were then soldered onto the leads. The kirigami platform was adhered to the body while the subject was standing in a neutral position, using the flexible adhesive fabric KT Tape. Markers were placed at specific locations on the subject's upper limbs for the camera motion tracking system. The subject, who is a co-author of the manuscript, was informed of all aspects of the tracking sensor testing and provided full consent.

Measurement of Tracking Sensor: The electrical resistance of each of the strain gauges was recorded using Agilent 4155 semiconductor parameter analyzer (3.3 V and 9.9 mA input). Simultaneously, the reflective markers on the body were tracked using a 19-camera motion capture system, Cortex, (Motion Analysis Corporation, Santa Rosa, CA) which captured data at

100 Hz.^[12] The joint angles were calculated in Visual 3D based on joint centers and local coordinate system as delineated in Engdahl's study.^[12]

Supporting Information

Supporting Information is available from the Wiley Online Library or from the author.

Acknowledgements

The authors thank Christina Lee and Dr. Susannah Engdahl, working under the supervisions of Prof. Deanna Gates in the departments of Biomedical Engineering and Kinesiology at the University of Michigan, for helping collect the angular position data using the camera tracking system and processing the data. Also, the authors thank Prof. Anthony Palazotto at the Air Force Institute of Technology who helped develop the FEA settings. Kevin Greenman and Tristan Blanzzy provided help for the CAD designs. The authors also acknowledge Dr. Aaron Lamoureux for developing the baseline circular cut pattern, Dr. Steve Morris, Brian Iezzi, Joanna Ciatti, and Sid Borsadia for insightful discussions. The authors thank the National Science Foundation (Grant NSF 1240264) under the Emerging Frontiers in Research and Innovation (EFRI) ODISSEI program. M.S. also acknowledges the support of the Weston Visiting Professorship in the department of Molecular Cell Biology, Weizmann Institute of Science, in the writing of this work.

Conflict of Interest

We have no financial conflict of interest in this paper. A patent has been submitted on the technology described in the manuscript.

Keywords

curved surfaces, kirigami, motion tracking, planar integration, wearable sensors

Received: July 3, 2019

Revised: September 12, 2019

Published online: October 15, 2019

- [1] R. C. Mather III, L. Koenig, D. Acevedo, T. M. Dall, P. Gallo, A. Romeo, J. Tongue, G. Williams Jr., *J. Bone Joint Sur.* **2013**, *95*, 1993.
- [2] S. W. Castillo, N. Lezin, in *The Burden of Musculoskeletal Diseases in the United States: Prevalence, Societal and Economic Cost*, 3rd ed., United States Bone and Joint Initiative, Rosemont, IL **2016**.
- [3] U. Gedalia, M. Solomonow, B. H. Zhou, R. V. Baratta, Y. Lu, M. Harris, *Spine* **1999**, *24*, 2461.
- [4] R. L. Gajdosik, R. W. Bohannon, *Phys. Ther.* **1987**, *67*, 1867.
- [5] A. Glynn, H. Fiddler, in *The Physiotherapist's Pocket Guide to Exercise*, Churchill Livingstone, Edinburgh **2009**.
- [6] K. H. Mcveigh, P. M. Murray, M. G. Heckman, B. Rawal, J. J. Peterson, *J. Hand Surg.* **2016**, *41*, e21.

- [7] E. M. Sluijs, G. J. Kok, J. van der Zee, *Phys. Ther.* **1993**, *73*, 771.
- [8] J. Heikenfeld, A. Jajack, J. Rogers, P. Gutruf, L. Tian, T. Pan, R. Li, M. Khine, J. Kim, J. Wang, J. Kim, *Lab Chip* **2018**, *18*, 217.
- [9] S. K. Subramanian, C. L. Massie, M. P. Malcolm, M. F. Levin, *Neurorehabil. Neural Repair* **2010**, *24*, 113.
- [10] Q. Wang, P. Markopoulos, B. Yu, W. Chen, A. Timmermans, *J. Neuroeng. Rehabil.* **2017**, <https://doi.org/10.1186/s12984-017-0229-y>.
- [11] D. H. Gates, L. S. Walters, J. Cowley, J. M. Wilken, L. Resnik, *Am. J. Occup. Ther.* **2015**, *70*, 7001350010p1.
- [12] S. M. Engdahl, D. H. Gates, *Gait Posture* **2018**, *60*, 41.
- [13] Y. Menguc, Y.-L. Park, E. Martinez-Villalpando, P. Aubin, M. Zisook, L. Stirling, R. J. Wood, C. J. Walsh, *Robotics and Automation (ICRA), 2013 IEEE Int. Conf.*, IEEE, Piscataway, NJ, May **2013**, p. 5309.
- [14] Y. C. Chen, H. J. Lee, K. H. Lin, *2015 37th Annual Int. Conf. of the IEEE EMBC*, Milan, Italy, August **2015**.
- [15] X. Robert-Lachaine, H. Mecheri, C. Larue, A. Plamondon, *Med. Biol. Eng. Comput.* **2017**, *55*, 609.
- [16] X. Tao, G. Wang, Y. Wang, H. Zhang, *US Patent 12,122,883*, **2008**.
- [17] Q. Wang, L. De Baets, A. Timmermans, W. Chen, L. Giacolini, T. Matheve, P. Markopoulos, *Sensors* **2017**, *17*, 1687.
- [18] S. Ma, T. Ye, T. Zhang, Z. Wang, K. Li, M. Chen, J. Zhang, Z. Wang, S. Ramakrishna, L. Wei, *Adv. Mater. Technol.* **2018**, *3*, 1800033.
- [19] M. Gholami, A. Ejupi, A. Rezaei, A. Ferrone, C. Menon, in *Proc. 2018 IEEE Int. Conf. on Biomedical Robotics and Biomechatronics (BioRob)* IEEE, Piscataway, NJ **2018**.
- [20] S. Seyedin, J. Razal, P. C. Innis, A. Jeiranikhameneh, S. Beirne, G. G. Wallace, *ACS Appl. Mater. Interfaces* **2015**, *7*, 21150.
- [21] F. Lorussi, N. Carbonaro, D. De Rossi, R. Paradiso, P. Veltink, A. Tognetti, *Front. Bioeng. Biotechnol.* **2016**, *4*, 28.
- [22] M. Blees, A. Barnard, P. Rose, S. Roberts, K. McGill, P. Huang, A. Ruyack, J. Kevek, B. Kobrin, D. Muller, P. McEuen, *Nature* **2015**, *524*, 204.
- [23] T. C. Shyu, P. F. Damasceno, P. M. Dodd, A. Lamoureux, L. Xu, M. Shlian, M. Shtein, S. C. Glotzer, N. A. Kotov, *Nat. Mater.* **2015**, *14*, 785.
- [24] L. Xu, T. C. Shyu, N. A. Kotov, *ACS Nano* **2017**, *11*, 7587.
- [25] Y.-S. Guan, H. Li, F. Ren, S. Ren, *ACS Nano* **2018**, *12*, 7967.
- [26] M. Isobe, K. Okumura, *Sci. Rep.* **2016**, *6*, 24758.
- [27] A. Rafsanjani, Y. Zhang, B. Liu, S. M. Rubinstein, K. Bertoldi, *Sci. Rob.* **2018**, *3*, eaar7555.
- [28] B. Kim, F. Liu, Y. Yu, H. Jang, Z. Xie, K. Li, J. Lee, J. Jeong, A. Ryu, Y. Lee, D. Kim, X. Wang, K. Lee, J. Lee, S. Won, N. Oh, J. Kim, J. Kim, S. Jeong, K. Jang, S. Lee, Y. Huang, Y. Zhang, J. Rogers, *Adv. Funct. Mater.* **2018**, *28*, 1803149.
- [29] Z. Yan, F. Zhang, F. Liu, M. Han, D. Ou, Y. Liu, Q. Lin, X. Guo, H. Fu, Z. Xie, M. Gao, Y. Huang, J. Kim, Y. Qiu, K. Nan, J. Kim, P. Gutruf, H. Luo, A. Zhao, K. Hwang, Y. Huang, Y. Zhang, J. Rogers, *Sci. Adv.* **2016**, *2*, e1601014.
- [30] Y. Yamamoto, S. Harada, D. Yamamoto, W. Honda, T. Arie, S. Akita, K. Takei, *Sci. Adv.* **2016**, *2*, e1601473.
- [31] B. Gao, A. Elbaz, Z. He, Z. Xie, H. Xu, S. Liu, E. Su, H. Liu, Z. Gu, *Adv. Mater. Technol.* **2018**, *3*, 1700308.
- [32] A. L. Lamoureux, *Origami and Kirigami Design Principles for Optical Tracking, Energy Harvesting, and Other Applications*, University of Michigan, Ann Arbor, MI **2017**.